DE GRUYTER Open Physics 2023; 21: 20230150

Research Article

Mohammed M. Babatin*, Mohamed M. Khader, and Ahmed M. Megahed

Numerical investigation of the flow characteristics involving dissipation and slip effects in a convectively nanofluid within a porous medium

https://doi.org/10.1515/phys-2023-0150
received September 15, 2023; accepted November 08, 2023

Abstract: The aim of the present research is to discuss the numerical aspects of heat-mass transfer in power-law nanofluids on an stretched surface. In addition, the novelty in this research lies in its thorough exploration and incorporation of parameters such as viscous dissipation, slip velocity, and convective boundary conditions into the analysis. This distinguishes the study from previous work and underscores its originality. For non-Newtonian fluids, a power-law model is employed, while the nanofluid system associate the influences of thermophoresis and the Brownian motion. The fluid's thermal conductivity is considered to change based on temperature, while the concentration of nanoparticles at the surface is maintained at a constant level. A heated fluid situated beneath the lower surface can act as a heat convection mechanism source. A process of similarity transformation is employed to simplify the equations related to the mass, momentum, thermal energy, and nanoparticle concentration into nonlinear ordinary differential equations. These equations are then treated numerically with the help of the shifted Chebyshev polynomials of the sixth order and the spectral collocation method. The proposed technique reduces the existing problem into a system of algebraic equations formulated as a constrained optimization challenge. Subsequently, the optimization technique is applied to determine the unknown coefficients of the series solution. Graphical representations depict the impacts of nanofluid parameters. A quantitative assessment is presented in a tabular format to illustrate a comparison with previously published results for specific scenarios, revealing a notable level of agreement.

Keywords: porous medium, nanofluid, convective boundary conditions, viscous dissipation, slip velocity, optimization-spectral collocation method, Chebyshev polynomials

Nomenclature

c	positive constant
C	nanofluid concentration
c_p	specific heat
C_w	concentration of the fluid beside the sheet
C_∞	concentration of the fluid at the ambient
Cf_x	skin friction coefficient
D_T	thermophoretic coefficient
D_B	diffusion coefficient
Ec	Eckert number
f	dimensionless stream function
h_f	coefficient of heat transfer
k	permeability of the porous medium
n	power-law index
N_t	thermophoresis parameter
N_b	Brownian motion parameter
Nu_x	Nusselt number
Pr	Prandtl number
Re	the local Reynolds number
s	exponent of stretching
Sc	Schmidt number
Sh_x	Sherwood number

*** Corresponding author: Mohammed M. Babatin,** Department of Mathematics and Statistics, College of Science, Imam Mohammad, Ibn Saud Islamic University (IMSIU), Riyadh 11566, Saudi Arabia, e-mail: mmbabatin@imamu.edu.sa
Mohamed M. Khader: Department of Mathematics and Statistics, College of Science, Imam Mohammad, Ibn Saud Islamic University (IMSIU), Riyadh 11566, Saudi Arabia; Department of Mathematics, Faculty of Science, Benha University, Benha, Egypt, e-mail: mmkhader@imamu.edu.sa
Ahmed M. Megahed: Department of Mathematics, Faculty of Science, Benha University, Benha, Egypt, e-mail: ahmed.abdelbaqk@fsc.bu.edu.eg

T	temperature of the nanofluid
T_f	temperature of the fluid below the sheet
T_w	sheet temperature
T_∞	temperature of the nanofluid away the sheet
U_w	stretching velocity
u, v	components of the velocity vector in the x- and y-directions, respectively
Greek symbols	
η	dimensionless variable
κ	nanofluid thermal conductivity
δ	porous parameter
ϕ	dimensionless nanofluid concentration
λ	slip velocity factor
ρ	nanofluid density
κ_∞	ambient nanofluid thermal conductivity
μ	nanofluid viscosity
τ	heat capacity ratio of the nanomaterial to that of the fluid
ε	thermal conductivity parameter
γ	Biot number
θ	dimensionless nanofluid temperature
λ_0	slip velocity coefficient
ψ	stream function
Superscripts	
w	condition along the sheet
$'$	differentiation with respect to η
∞	condition at the ambient

1 Introduction

Flow of the Newtonian fluids across an elastic sheets is encountered in various engineering procedures that find use in industries. These applications encompass processes like extrusion, melt-spinning, hot rolling, production of glass-fibers, and cooling of substantial metal plates in a bath, among others [1]. Non-Newtonian fluids constitute a broad spectrum of significant models, among which are notable examples such as the Casson model [2], Maxwell system [3], micropolar system [4], Williamson system [5], Walter's B model [6], and the tangent hyperbolic model [7] and [8], to name a few. A non-Newtonian power law fluid (PLF) is a complex substance that deviates from the linear correlation between shear rate and shear stress found in Newtonian fluids [9]. This type of fluids exhibits a behavior that conforms to a power law connection, wherein the shear stress is directly related to the shear rate raised to a specific exponent, referred to as the flow behavior index [10]. This exponent dictates the extent of the fluid's shear-thinning or shear-thickening characteristics. In simpler terms, the viscosity of a non-Newtonian PLW can undergo substantial changes as the shear rate varies [11]. Power-law models are commonly encountered in a wide range of industrial and biological settings. These models find practical applications in various fields, including food manufacturing, coatings, polymers, and even bodily fluids like blood, as mentioned in the study by Sui *et al.* [12]. Moreover, they play a crucial role in understanding and controlling physical phenomena such as viscous dissipation, thermal radiation, and magnetic fields within the context of heat-mass transfer processes. Obtaining a deeper understanding of the flow behavior of non-Newtonian PLWs is imperative for improving processes and optimizing designs across these diverse domains [13].

The expression "nanofluid" pertains to a liquid that includes a dispersion of submicron solid particles, commonly known as nanoparticles. Choi [14] is credited with coining this term. The defining trait of nanofluids is the augmentation of thermal conductivity, an occurrence initially observed by Masuda *et al.* [15]. Aziz and Khan [16] noted that a satisfactory elucidation for the anomalous rise in thermal conductivity and viscosity remains elusive. Numerous researchers have investigated the boundary layer (BL) flow generated by the stretching of an elastic sheet in various nanofluid models, resulting in a substantial body of literature dedicated to this particular issue [17].

Building upon previous investigations, many researchers have effectively employed diverse numerical methodologies in this specific field. One such method is the spectral collocation technique (SCM), which stands as a versatile approximate analytical approach for deriving approximate solutions to differential equations. The SCM presents several merits in tackling such issues, as the Chebyshev coefficients of the solution can be easily computed using any accessible numerical software, resulting in superior computational efficiency [18]. Chebyshev polynomials, recognized orthogonal polynomials defined within the domain $[-1, 1]$, are commonly utilized due to their advantageous characteristics in approximating functions. Furthermore, this approach is distinguished by its remarkable precision, rendering it a dependable numerical method. With its capacity to ensure precise calculations and dependable results, the technique guarantees swift convergence rates and straightforward application in a variety of problem contexts, spanning finite and infinite domains, as demonstrated in the previous work [19]. It exhibits rapid convergence, enabling accurate solutions to be attained with a few number of terms, effectively conserving computational resources and time. In addition, the method's flexibility permits its utilization not only in differential equations but also in optimization problems, establishing its value across a wide array of domains [20]. This method has been extensively utilized in different problems [21] and has played a significant role in conducting crucial research owing to these benefits.

According to the author's current knowledge, the literature has not yet addressed this particular aspect. The purpose of investigating these studies on power-law nanofluids is to provide an accurate representation of the transport properties of the nanofluid. Moreover, what sets this research apart is its comprehensive investigation and integration of factors like new mass flux condition, viscous dissipation, slip velocity, and convective boundary conditions within the analysis. This serves to differentiate the study from earlier research and emphasizes its novelty. An optimization method utilizing sixth-kind Chebyshev polynomials is employed to visually illustrate the impact of these properties through tables and graphs.

2 Formulation of the physical model

Assume the consistent two-dimensional BL movement of a non-Newtonian PLF with nanoparticles over an extending sheet, featuring a nonlinear velocity distribution of $U_w = cx^s$. In this formula, c represents a constant, s is the stretching factor, and x denotes the position along the stretching surface. It is considered that the sheet is enclosed within a porous medium possessing permeability denoted as k. The lower side of the surface is subjected to heating as fluid flows over it at a temperature of T_f. This heating process involves varying heat transfer coefficient h_f, and it operates through a convective heat transfer mechanism. The extended sheet is held at an unchanging temperature T_w, and a consistent concentration C_w. Furthermore, the uniformity of ambient temperature and concentration, denoted as T_∞, and C_∞, respectively, is presumed at a significant distance away from the sheet's surface. Furthermore, it is taken into consideration that T_f is greater than T_w, and T_w is greater than T_∞. The visual representation in Figure 1 illustrates the flow of a power law nanofluid initiated by a nonlinearly stretching sheet within a porous medium.

The non-Newtonian fluid employs the power-law model, which defines the connection between strain rate and shear stress as follows [22]:

$$\tau_{xy} = \mu\left(-\frac{\partial u}{\partial y}\right)^{n-1}\frac{\partial u}{\partial y}, \tag{1}$$

where n denotes the power law exponent. When n equals 1, formula (1) characterizes a Newtonian fluid featuring a dynamic viscosity coefficient of μ. Conversely, when n is greater than 1, formula (1) describes a dilatant or shear-thickening fluid, and when n is less than 1, it portrays a pseudoplastic or shear-thinning fluid. Moreover, the thermal conductivity κ of PLF is taken to change as it moves, and this change adheres to a linear relationship with temperature. This temperature-related connection can be formulated in the subsequent manner [23]:

$$\kappa = \left[\kappa_\infty + \varepsilon\left[\kappa_\infty\left(\frac{T - T_\infty}{T_f - T_\infty}\right)\right]\right]. \tag{2}$$

Evidently, based on the recent equation, the thermal conductivity remains consistent at ambient conditions $T = T_\infty$ and reaches its peak value when the temperature equals $T = T_f$, where T is the PLF temperature and κ_∞ represents the ambient thermal conductivity. In the energy equation, we

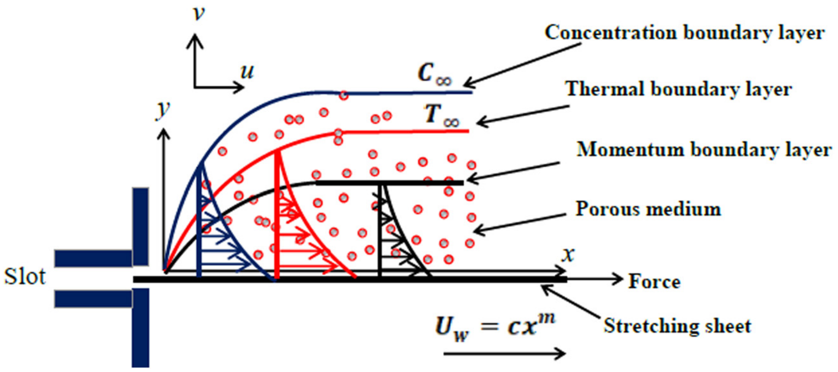

Figure 1: A sketch of the physical model.

consider the inclusion of viscous dissipation using the power-law model, as well as the impacts of thermophoresis phenomenon and the Brownian motion of nanoparticles. By employing scale analysis, the governing equations for momentum, mass, thermal energy, and nanoparticles concentration in power-law nanofluid model will be expressed in Cartesian coordinates x and y in the following form [24] ($\nabla = (\frac{\partial}{\partial x}, \frac{\partial}{\partial y})$):

$$\nabla\cdot(u, v) = 0, \tag{3}$$

$$(u, v)\cdot\nabla u = \frac{\mu}{\rho}\frac{\partial}{\partial y}\left(\left(-\frac{\partial u}{\partial y}\right)^{n-1}\frac{\partial u}{\partial y}\right) - \frac{\mu}{\rho k}u, \tag{4}$$

$$\begin{aligned}(u, v)\cdot\nabla T - \tau\left[D_B\frac{\partial T}{\partial y}\frac{\partial C}{\partial y} + \frac{D_T}{T_\infty}\left(\frac{\partial T}{\partial y}\right)^2\right] \\ = \frac{1}{\rho c_p}\frac{\partial}{\partial y}\left(\kappa\frac{\partial T}{\partial y}\right) + \frac{\mu}{\rho c_p}\left(-\frac{\partial u}{\partial y}\right)^{n+1},\end{aligned} \tag{5}$$

$$(u, v)\cdot\nabla C = D_B\frac{\partial^2 C}{\partial y^2} + \frac{D_T}{T_\infty}\frac{\partial^2 T}{\partial y^2}, \tag{6}$$

where ρ denotes the density of the fluid, D_B represents the coefficient of Brownian motion, and D_T is the thermophoresis diffusion coefficient. The suitable boundary conditions for the velocity, temperature, and concentration fields in the current scenario are provided as follows [25]:

$$\begin{aligned}u = U_w + \lambda_0\left[\left(-\frac{\partial u}{\partial y}\right)^{n-1}\frac{\partial u}{\partial y}\right], \\ -\kappa\left(\frac{\partial T}{\partial y}\right) = h_f(T_f - T_w), \quad \text{at } y = 0,\end{aligned} \tag{7}$$

$$v = 0, \quad D_B\frac{\partial C}{\partial y} + \frac{D_T}{T_\infty}\frac{\partial T}{\partial y} = 0, \quad \text{at } y = 0, \tag{8}$$

$$u \to 0, \quad C \to C_\infty, \quad T \to T_\infty \quad \text{as}, \ y \to \infty, \tag{9}$$

where λ_0 is the coefficient of slip velocity. As outlined by Mahmoud and Megahed [24], we employ the subsequent transformations [24]:

$$\begin{aligned}\psi(\eta) = (\nu)^{\frac{1}{n+1}}c^{\frac{2n-1}{n+1}}x^{\frac{s(2n-1)+1}{n+1}}f(\eta), \\ \eta = \left[(\nu)^{\frac{-1}{n+1}}c^{\frac{2-n}{n+1}}x^{\frac{s(2-n)-1}{n+1}}\right]y,\end{aligned} \tag{10}$$

$$\theta(\eta) = \frac{T - T_\infty}{T_f - T_\infty}, \quad \phi(\eta) = \frac{C - C_\infty}{C_w - C_\infty}, \tag{11}$$

where $\nu = \frac{\mu}{\rho}$ is the kinematic viscosity and η is the similarity variable. Also, in the aforementioned equations, ψ denotes the stream function, which satisfies the continuity Eq. (3), and defines by the following:

$$u = \frac{\partial\psi}{\partial y}, \quad v = -\frac{\partial\psi}{\partial x}. \tag{12}$$

By making use of the similarity transformations as described in Eqs. (10) and (11), we can precisely fulfill the continuity Eq. (3). In addition, Eqs. (4)–(6) are modified into the subsequent formulations:

$$nf'''(-f'')^{n-1} + \left(\frac{s(2n-1)+1}{n+1}\right)ff'' - sf'^2 - \delta f' = 0, \tag{13}$$

$$\begin{aligned}\left[\frac{(1 + \varepsilon\theta)\theta'' + \varepsilon\theta'^2}{\Pr}\right] + N_t\theta'^2 + N_b\theta'\phi' \\ + \left(\frac{s(2n-1)+1}{n+1}\right)f\theta' + \mathrm{Ec}(-f'')^{n+1} = 0,\end{aligned} \tag{14}$$

$$\phi'' + \frac{N_t}{N_b}\theta'' + \mathrm{Sc}\left(\frac{s(2n-1)+1}{n+1}\right)f\phi' = 0. \tag{15}$$

Likewise, the adjusted boundary conditions are stated as follows:

$$\begin{aligned}\eta = 0 : f = 0, \quad f' = 1 + \lambda[f''(-f'')^{n-1}], \\ \theta' = -\gamma\left[\frac{1-\theta}{1+\varepsilon\theta}\right], \quad N_t\theta' + N_b\phi' = 0,\end{aligned} \tag{16}$$

$$\eta \to \infty : f' \to 0, \quad \theta \to 0, \ \phi \to 0, \tag{17}$$

where the parameters $\delta, \lambda, \mathrm{Ec}, \gamma, \mathrm{Sc}, \Pr, N_b,$ and N_t, are defined as follows:

$$\begin{aligned}\delta = \frac{\mu}{\rho k U_w}x, \quad \lambda = \lambda_0\left(\frac{c^{2-n}x^{s(2-n)-1}}{\nu}\right)^{\frac{n}{n+1}}, \\ \mathrm{Ec} = \frac{U_w^2}{c_p(T_f - T_\infty)}, \quad \gamma = \frac{xh_f}{\kappa_\infty}\mathrm{Re}_x^{\frac{-1}{n+1}}, \quad \mathrm{Sc} = \frac{\nu}{D_B}, \\ \Pr = \frac{\rho c_p}{\kappa_\infty}(x^{(3s-1)(n-1)}c^{3(n-1)}(\nu)^2)^{\frac{1}{n+1}}, \\ N_b = \frac{\tau D_B(C_w - C_\infty)}{\nu}, \\ N_t = \frac{\tau D_T(T_f - T_\infty)}{\nu T_\infty}.\end{aligned} \tag{18}$$

3 Quantities relevant to engineering and industry

The dimensionless variables that are of practical importance encompass the friction factor Cf_x, local Sherwood number Sh_x, and local Nusselt number Nu_x. These parameters are elucidated as follows:

$$\begin{aligned}Cf_x = -2\mathrm{Re}_x^{\frac{-1}{n+1}}(-f''(0))^n, \quad \mathrm{Sh}_x = -\mathrm{Re}_x^{\frac{1}{n+1}}\phi'(0), \\ \mathrm{Nu}_x = -\mathrm{Re}_x^{\frac{1}{n+1}}\theta'(0),\end{aligned}$$

where $\mathrm{Re}_x = \frac{U_w^{2-n}x^n}{\nu}$ is the local power-law Reynolds number.

4 Procedure of solution using SCM

4.1 Some properties of the CP$_6$s and approximate the solution

We present some of the main definitions and properties of the shifted Chebyshev polynomials of the sixth-kind (CP$_6$s) [26] to suit their use in solving the problem under study in the domain $[0, \hbar]$.

With the help of the following recurrence relation, we can generate the orthogonal Chebyshev polynomials $T_k(z)$ [27,28]:

$$T_k(z) = zT_{k-1}(z) - \left(\frac{(-1)^k(2k+1) + k(k+1) + 1}{4k(k+1)}\right)T_{k-2}(z),$$

$$T_0(z) = 1, \quad T_1(z) = z, \;\; k = 2, 3, \ldots$$

The shifted CP$_6$s on $[0, \hbar]$, $\hbar > 0$ can be defined with the help of the linear transformation $z = (2/\hbar)\eta - 1$ as $\mathbb{T}_k(\eta) = T_k((2/\hbar)\eta - 1)$ [29]. We can obtain the polynomials $\{\mathbb{T}_k(\eta)\}_{k=0}^{\infty}$ by the following recursive formula [30]:

$$\begin{aligned}\mathbb{T}_k(\eta) &= ((2/\hbar)\eta - 1)\mathbb{T}_{k-1}(\eta)\\ &\quad - \left(\frac{(-1)^k(2k+1) + k(k+1) + 1}{4k(k+1)}\right)\mathbb{T}_{k-2}(\eta),\\ &\quad k = 2, 3, \ldots,\end{aligned}$$

where $\mathbb{T}_0(\eta) = 1$, $\mathbb{T}_1(\eta) = (2/\hbar)\eta - 1$.

The analytic formula of $\mathbb{T}_k(\eta)$ is given by [31]:

$$\mathbb{T}_k(\eta) = \sum_{i=0}^{k} c_{i,k}\eta^i, \tag{19}$$

where

$$c_{i,k} = \frac{2^{2i-k}}{\hbar^i(2i+1)!}\begin{cases}\displaystyle\sum_{r=\lfloor\frac{i+1}{2}\rfloor}^{\lfloor\frac{k}{2}\rfloor}\frac{(-1)^{0.5k+r+i}(2r+i+1)!}{(2r-i)!}, & \text{if } k \text{ even},\\[2ex] \displaystyle\sum_{r=\lfloor\frac{i}{2}\rfloor}^{\lfloor\frac{k-1}{2}\rfloor}\frac{2(-1)^{0.5(k+1)+r+i}(r+1)(2r+i+2)!}{(k+1)(2r-i+1)!}, & \text{if } k \text{ odd}.\end{cases}$$

The function $\psi(\eta) \in L_2[0, \hbar]$ can be approximated as a finite series sum with the first $(m+1)$-terms as follows:

$$\psi_m(\eta) = \sum_{\ell=0}^{m}\zeta_\ell\mathbb{T}_\ell(\eta). \tag{20}$$

Through the following two theorems, respectively, we investigate the upper bound of the error in the approximation by using the CP$_6$s and drive the main approximate formula of the derivatives for the approximation solution $\psi_m(\eta)$.

Theorem 1. [21] *The obtained truncation error* $\varepsilon_m = |\psi(\eta) - \psi_m(\eta)|$ *in approximating the function* $\psi(\eta)$ *by* $\psi_m(\eta)$, *which is defined in* (20) *can be estimated as follows*:

$$\varepsilon_m \le 2^{-m}.$$

Theorem 2. *Let* $\psi(\eta)$ *be approximated by* CP$_6$s *as* (20), $n > 0$, *then*:

$$\psi_m^{(n)}(\eta) \simeq \sum_{i=n}^{m}\sum_{k=n}^{i}\zeta_i\chi_{i,k,n}\eta^{k-n}, \tag{21}$$

where $\chi_{i,k,n} = (k!/(k-n)!)c_{i,k}$, *but* $c_{i,k}$ *is defined in Eq.* (19).

Proof. Due to the differentiation operator is linear, we can obtain the following:

$$\psi_m^{(n)}(\eta) = \sum_{i=0}^{m}\zeta_i D^{(n)}(\mathbb{T}_i(\eta)). \tag{22}$$

Now, we find:

$$D^{(n)}\mathbb{T}_i(\eta) = 0, \quad i = 0, 1, \ldots, n-1. \tag{23}$$

Also, for $i = n, n+1, \ldots, m$, we can obtain:

$$D^{(n)}(\mathbb{T}_i(\eta)) = \sum_{k=n}^{i}c_{i,k}D^{(n)}\eta^k = \sum_{k=n}^{i}c_{i,k}\frac{k!}{(k-n)!}\eta^{k-n}. \tag{24}$$

The connection with Eqs. (22)–(24) leads us to obtain the desired formula (21). ☐

4.2 Approximate the solution with a numerical scheme

In this subsection, we are going to implement the SCM for solving numerically the proposed system (13)–(17). We approximate $f(\eta)$, $\theta(\eta)$, and $\phi(\eta)$ by $f_m(\eta)$, $\theta_m(\eta)$, and $\phi_m(\eta)$, respectively, in the following forms:

$$\begin{aligned} f_m(\eta) &= \sum_{\ell=0}^{m}a_\ell\mathbb{T}_\ell(\eta), \quad \theta_m(\eta) = \sum_{\ell=0}^{m}b_\ell\mathbb{T}_\ell(\eta),\\ \phi_m(\eta) &= \sum_{\ell=0}^{m}c_\ell\mathbb{T}_\ell(\eta).\end{aligned} \tag{25}$$

The substituting from (21) and (25) in the system (13)–(15) leads us to obtain the following system:

$$\begin{aligned} &nf_m^{(3)}(\eta)(-f_m^{(2)}(\eta))^{n-1} + \left(\frac{s(2n-1)+1}{n+1}\right)(f_m(\eta))(f_m^{(2)}(\eta))\\ &\quad - s(f_m^{(1)}(\eta))^2 - \delta(f_m^{(1)}(\eta)) = 0,\end{aligned} \tag{26}$$

$$\begin{aligned}&\left(\frac{1}{\mathrm{Pr}}\right)((1+\varepsilon\theta_m(\eta))(\theta_m^{(2)}(\eta))+\varepsilon(\theta_m^{(1)}(\eta))^2)+N_t(\theta_m^{(1)}(\eta))^2\\&\quad+N_b(\theta_m^{(1)}(\eta))(\phi_m^{(1)}(\eta))+\left(\frac{s(2n-1)+1}{n+1}\right)(f_m(\eta))(\theta_m^{(1)}(\eta))\\&\quad+\mathrm{Ec}(-(f_m^{(2)}(\eta)))^{n+1}=0,\end{aligned}\tag{27}$$

$$\begin{aligned}&\phi_m^{(2)}(\eta)+\frac{N_t}{N_b}(\theta_m^{(2)}(\eta))\\&\quad+\mathrm{Sc}\left(\frac{s(2n-1)+1}{n+1}\right)(f_m(\eta))(\phi_m^{(1)}(\eta))=0.\end{aligned}\tag{28}$$

We collocate the previous Eqs. (26)–(28) at m of nodes η_p to reduce it to the following nonlinear algebraic equations:

$$\begin{aligned}&nf_m^{(3)}(\eta_p)(-f_m^{(2)}(\eta_p))^{n-1}\\&\quad+\left(\frac{s(2n-1)+1}{n+1}\right)(f_m(\eta_p))(f_m^{(2)}(\eta_p))-s(f_m^{(1)}(\eta_p))^2\\&\quad-\delta(f_m^{(1)}(\eta_p))=0,\end{aligned}\tag{29}$$

$$\begin{aligned}&\left(\frac{1}{\mathrm{Pr}}\right)((1+\varepsilon\theta_m(\eta_p))(\theta_m^{(2)}(\eta_p))+\varepsilon(\theta_m^{(1)}(\eta_p))^2)\\&\quad+N_t(\theta_m^{(1)}(\eta_p))^2+N_b(\theta_m^{(1)}(\eta_p))(\phi_m^{(1)}(\eta_p))\\&\quad+\left(\frac{s(2n-1)+1}{n+1}\right)(f_m(\eta_p))(\theta_m^{(1)}(\eta_p))\\&\quad+\mathrm{Ec}(-(f_m^{(2)}(\eta_p)))^{n+1}=0,\end{aligned}\tag{30}$$

$$\begin{aligned}&\phi_m^{(2)}(\eta_p)+\frac{N_t}{N_b}(\theta_m^{(2)}(\eta_p))\\&\quad+\mathrm{Sc}\left(\frac{s(2n-1)+1}{n+1}\right)(f_m(\eta_p))(\phi_m^{(1)}(\eta_p))=0.\end{aligned}\tag{31}$$

Also, the boundary conditions (16)–(17) will be reduced to the following algebraic equations by substituting from Eq. (25) in Eqs. (16)–(17):

$$\begin{aligned}&\sum_{\ell=0}^{m}2(-1)^{\ell}a_{\ell}=0,\\&\sum_{\ell=0}^{m}a_{\ell}\mathbb{T}'_{\ell}(0)=1+\lambda\left[\sum_{\ell=0}^{m}a_{\ell}\mathbb{T}'_{\ell}(0)\left(-\sum_{\ell=0}^{m}a_{\ell}\mathbb{T}'_{\ell}(0)\right)^{n-1}\right],\\&\sum_{\ell=0}^{m}b_{\ell}\mathbb{T}'_{\ell}(0)=-\gamma\left[1-\sum_{\ell=0}^{m}2(-1)^{\ell}b_{\ell}\right]\left[1+\varepsilon\sum_{\ell=0}^{m}2(-1)^{\ell}b_{\ell}\right]^{-1},\\&N_t\sum_{\ell=0}^{m}b_{\ell}\mathbb{T}'_{\ell}(0)+N_b\sum_{\ell=0}^{m}c_{\ell}\mathbb{T}'_{\ell}(0)=0,\end{aligned}\tag{32}$$

$$\sum_{\ell=0}^{m}a_{\ell}\mathbb{T}'_{\ell}(\eta_{\infty})=0,\quad\sum_{\ell=0}^{m}2b_{\ell}=0,\quad\sum_{\ell=0}^{m}2c_{\ell}=0.\tag{33}$$

Now, we define the following cost functions to express the nonlinear system of $3(m+1)$ algebraic Eqs. (29)–(33) as a constrained optimization problem:

$$\begin{aligned}CF1=\sum_{p=0}^{m}\Bigg|&nf_m^{(3)}(\eta_p)(-f_m^{(2)}(\eta_p))^{n-1}\\&+\left(\frac{s(2n-1)+1}{n+1}\right)(f_m(\eta_p))(f_m^{(2)}(\eta_p))\\&-s(f_m^{(1)}(\eta_p))^2-\delta(f_m^{(1)}(\eta_p))\Bigg|,\end{aligned}\tag{34}$$

$$\begin{aligned}CF2=\sum_{p=0}^{m}\Bigg|&\left(\frac{1}{\mathrm{Pr}}\right)((1+\varepsilon\theta_m(\eta_p))(\theta_m^{(2)}(\eta_p))+\varepsilon(\theta_m^{(1)}(\eta_p))^2)\\&+N_b(\theta_m^{(1)}(\eta_p))(\phi_m^{(1)}(\eta_p))+N_t(\theta_m^{(1)}(\eta_p))^2\\&+\left(\frac{s(2n-1)+1}{n+1}\right)(f_m(\eta_p))(\theta_m^{(1)}(\eta_p))\\&+\mathrm{Ec}(-(f_m^{(2)}(\eta_p)))^{n+1}\Bigg|,\end{aligned}\tag{35}$$

$$\begin{aligned}CF3=\sum_{p=0}^{m}\Bigg|&\phi_m^{(2)}(\eta_p)+\frac{N_t}{N_b}(\theta_m^{(2)}(\eta_p))\\&+\mathrm{Sc}\left(\frac{s(2n-1)+1}{n+1}\right)(f_m(\eta_p))(\phi_m^{(1)}(\eta_p))\Bigg|,\end{aligned}\tag{36}$$

with the constraints (Cons):

$$\begin{aligned}\mathrm{Cons}=&\left|\sum_{\ell=0}^{m}2(-1)^{\ell}a_{\ell}\right|+\Bigg|\sum_{\ell=0}^{m}a_{\ell}\mathbb{T}'_{\ell}(0)-1\\&-\lambda\left[\sum_{\ell=0}^{m}a_{\ell}\mathbb{T}'_{\ell}(0)\left(-\sum_{\ell=0}^{m}a_{\ell}\mathbb{T}'_{\ell}(0)\right)^{n-1}\right]\Bigg|\\&+\Bigg|\sum_{\ell=0}^{m}b_{\ell}\mathbb{T}'_{\ell}(0)+\gamma\left[1\right.\\&\left.-\sum_{\ell=0}^{m}2(-1)^{\ell}b_{\ell}\right]\left[1+\varepsilon\sum_{\ell=0}^{m}2(-1)^{\ell}b_{\ell}\right]^{-1}\Bigg|\\&+\left|N_t\sum_{\ell=0}^{m}b_{\ell}\mathbb{T}'_{\ell}(0)+N_b\sum_{\ell=0}^{m}c_{\ell}\mathbb{T}'_{\ell}(0)\right|\\&+\left|\sum_{\ell=0}^{m}a_{\ell}\mathbb{T}'_{\ell}(\eta_{\infty})\right|+\left|\sum_{\ell=0}^{m}2b_{\ell}\right|+\left|\sum_{\ell=0}^{m}2c_{\ell}\right|.\end{aligned}\tag{37}$$

The constrained optimization problems (34)–(37) can be solved by using the Penalty Leap Frog procedure [32] for the coefficients $a_{\ell}, b_{\ell}, c_{\ell}$, and $\ell=0,1,\ldots,m$. By substituting these coefficients in the forms, (25) leads us to formulate the required approximate solution of the system under study (13)–(17).

Finally, to achieve a complete numerical simulation and estimate the efficiency of the proposed technique, we use the residual error function $\mathrm{REF}_f(\eta), \mathrm{REF}_\theta(\eta)$, and $\mathrm{REF}_\phi(\eta)$, of $f(\eta)$, $\theta(\eta)$, and $\phi(\eta)$, respectively:

$$\begin{aligned}\mathrm{REF}_f(m,\eta) = {} & nf_m^{(3)}(\eta)(-f_m^{(2)}(\eta))^{n-1} \\ & + \left(\frac{s(2n-1)+1}{n+1}\right)(f_m(\eta))(f_m^{(2)}(\eta)) \\ & - (f_m^{(1)}(\eta))^2 - \delta(f_m^{(1)}(\eta)),\end{aligned} \tag{38}$$

$$\begin{aligned}\mathrm{REF}_\theta(m,\eta) = {} & \left(\frac{1}{\mathrm{Pr}}\right)((1+\varepsilon\theta_m(\eta))(\theta_m^{(2)}(\eta)) \\ & + \varepsilon(\theta_m^{(1)}(\eta))^2) + N_t(\theta_m^{(1)}(\eta))^2 \\ & + N_b(\theta_m^{(1)}(\eta))(\phi_m^{(1)}(\eta)) \\ & + \mathrm{Ec}(-(f_m^{(2)}(\eta)))^{n+1} \\ & + \left(\frac{s(2n-1)+1}{n+1}\right)(f_m(\eta))(\theta_m^{(1)}(\eta)),\end{aligned} \tag{39}$$

$$\begin{aligned}\mathrm{REF}_\phi(m,\eta) = {} & \phi_m^{(2)}(\eta) + \frac{N_t}{N_b}(\theta_m^{(2)}(\eta)) \\ & + \mathrm{Sc}\left(\frac{s(2n-1)+1}{n+1}\right)(f_m(\eta))(\phi_m^{(1)}(\eta)).\end{aligned} \tag{40}$$

5 Validation of the code's accuracy

In this section, our goal is to verify the effectiveness of the provided numerical solution that has been applied in this context. Disregarding the influences of slip velocity and porous parameters ($\lambda = \delta = 0$) and setting the stretching factor to a unity value ($s = 1$), we compare the outcomes for the dimensionless wall shear stress $-f''(0)$ with the findings of Hassanien *et al.* [33] and Khan and Gorla [34] for various values of n in Table 1. The analysis reveals a strong concurrence for every power law index parameter in the comparison, affirming our high level of confidence in the precision of the current findings.

Table 1: Comparison the values of $-f''(0)$ in relation to the preceding research of [33] and [34] for various values of n when $\lambda = \delta = 0$ and $s = 1$

n	Work [33]	Work [34]	Present work
0.5	1.165235	1.161360	1.16135898
1.0	1.000000	1.000000	1.00000000
1.5	0.980902	0.980010	0.98000580

Table 2: Comparison the values of the REF obtained by the proposed scheme

η	REF of $f(\eta)$	REF of $\theta(\eta)$	REF of $\phi(\eta)$
0.0	1.852951×10^{-8}	2.021354×10^{-8}	0.015975×10^{-8}
1.0	7.951753×10^{-8}	5.654201×10^{-7}	2.357410×10^{-7}
2.0	6.852650×10^{-7}	4.095230×10^{-6}	3.652104×10^{-7}
3.0	2.963741×10^{-7}	2.982140×10^{-7}	0.752014×10^{-8}
4.0	3.789654×10^{-7}	9.632501×10^{-7}	2.321045×10^{-8}
5.0	0.951047×10^{-7}	3.852201×10^{-8}	7.855214×10^{-7}
6.0	7.963012×10^{-8}	7.952014×10^{-7}	4.662240×10^{-6}
7.0	6.875421×10^{-6}	5.852014×10^{-6}	3.875421×10^{-6}
8.0	4.021345×10^{-7}	0.952014×10^{-6}	2.632501×10^{-8}
9.0	3.6540123×10^{-7}	7.654127×10^{-7}	5.214570×10^{-8}
10.0	4.855201×10^{-6}	3.852147×10^{-6}	6.0145822×10^{-7}

Through Table 2, we presented the evaluated values of the residual error function (REF) for the purpose of verifying the validity of the approximate method used, where the values of the parameters are taken $\lambda = \delta = \gamma = \mathrm{Ec} = 0.2$, $\varepsilon = N_t = 0.1$, $N_b = 0.8$, $n = 1.2$, $s = 1/3$, $\mathrm{Sc} = 2.0$, $\mathrm{Pr} = 3.0$. In light of these values, we can confirm the accuracy of the technique proposed in this article.

6 Discussion of numerical results

The main aim of this study is to investigate how newly emerging physical parameters affect the temperature, velocity, and concentration profiles. Figure 2 delves into the discussion surrounding how changes in physical attributes, like the porous parameter δ, impact the profiles of velocity $f'(\eta)$, temperature $\theta(\eta)$, and concentration $\phi(\eta)$. As anticipated, an increase in the porous parameter results in a reduction of the momentum boundary layer thickness, concurrently leading to a decrease in velocity. Conversely, when the porous parameter is increased, it results in an elevation of both $\theta(\eta)$, and $\phi(\eta)$ levels for the same parameter value. Physically, the nanofluid concentration rises as the δ increases due to the greater porosity of the medium. This increased porosity facilitates improved nanoparticle transport and dispersion, allowing the fluid to hold more nanoparticles. Consequently, the nanofluid concentration within the porous medium increases, reflecting the influence of the δ on nanoparticle retention and distribution. Moreover, the findings in previously published research [35] validate the current observations regarding the flow and heat transfer characteristics within a porous medium.

Figure 3 illustrates how variations in the power-law index parameter n impact on $f'(\eta)$, $\theta(\eta)$, and $\phi(\eta)$. With an increasing power-law index parameter, both the

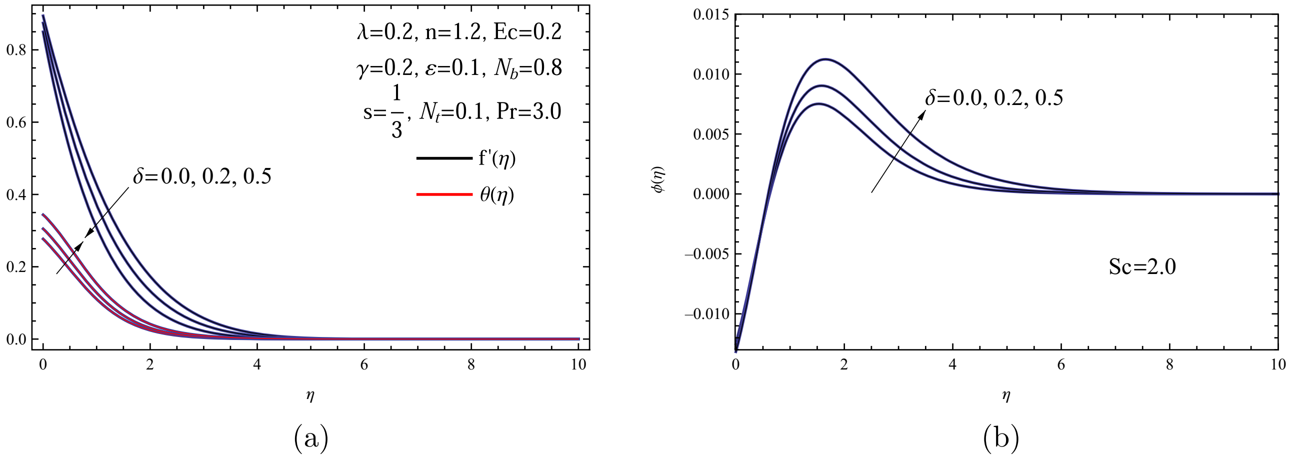

Figure 2: (a) $f'(\eta)$ and $\theta(\eta)$ for various δ (b) $\phi(\eta)$ for various δ.

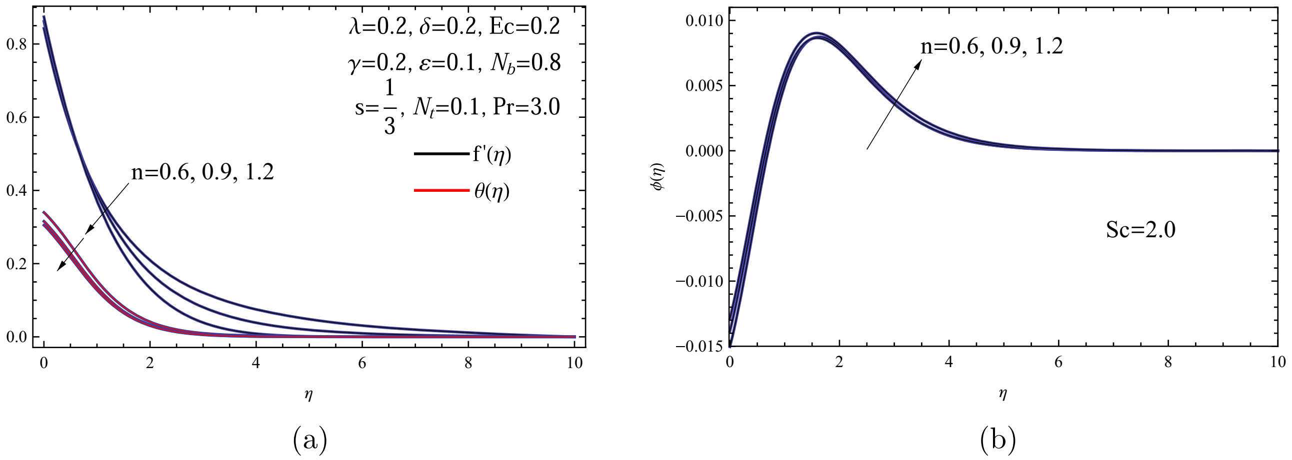

Figure 3: (a) $f'(\eta)$ and $\theta(\eta)$ for various n and (b) $\phi(\eta)$ for various n.

dimensionless temperature and dimensionless velocity decrease and converge toward a limit as the parameter approaches infinity. Physically, the nanofluid's velocity decreases as the power-law index parameter increases because the fluid becomes more non-Newtonian. In non-Newtonian fluids, higher values of this parameter indicate increased resistance to flow, leading to slower velocity. Physically, when the power-law index parameter is higher, it signifies a nanofluid that is thicker and exhibits increased viscosity, leading to a reduction in the flow velocity. In addition, it is worth noting that a marginal uptick in nanoparticle concentration has been observed under these identical parameter conditions.

Figure 4 examines how the slip velocity parameter λ affects the distributions of temperature $\theta(\eta)$, velocity $f'(\eta)$, and nanoparticle volume fraction $\phi(\eta)$ in the scenario involving a nonlinear stretching sheet. Examining the graphical representation reveals that when the slip velocity parameter increases, it causes both the temperature and velocity distributions to decrease. However, the opposite trend is observed when it comes to the concentration, particularly at a distance from the sheet.

Figure 5 shows how the Biot number influences the $\theta(\eta)$ and $\phi(\eta)$ fields. When the Biot number rises, it amplifies the thermal diffusivity, thereby necessitating the expansion of the thermal boundary layer (TBL). Physically, the Biot number tends to slow down the heat transfer from the solid surface to the fluid, which can lead to the observation of elevated temperatures near the surface, as depicted in the figure. It is important to note that the negative values of the concentration arises from its definition. Specifically, when the concentration of nanoparticles is higher at points away from the sheet compared to the concentration at any given point, this leads to a negative value for the

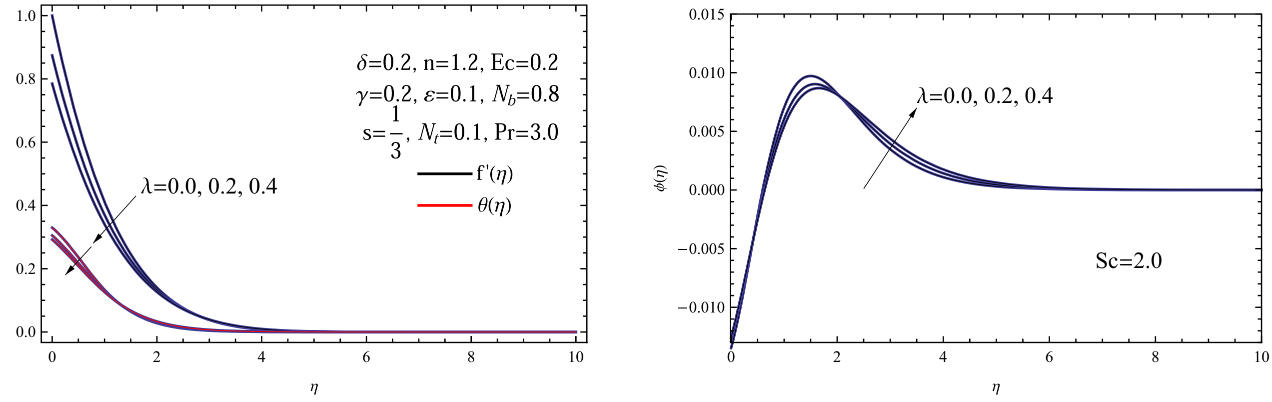

(a) (b)

Figure 4: (a) $f'(\eta)$ and $\theta(\eta)$ for various λ and (b) $\phi(\eta)$ for various λ.

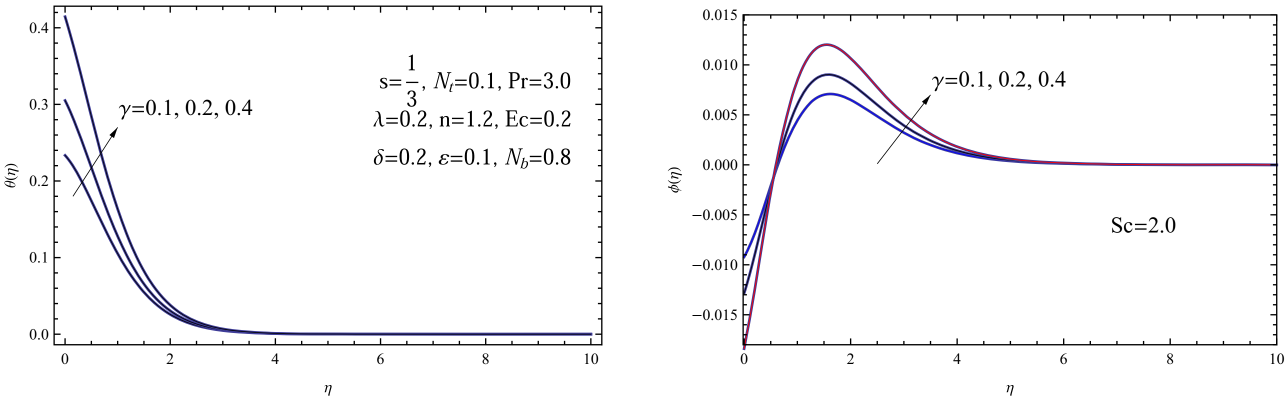

(a) (b)

Figure 5: (a) $\theta(\eta)$ for various γ and (b) $\phi(\eta)$ for various γ.

dimensionless concentration. Physically, a decrease in the Biot number has the potential to result in a higher concentration of nanoparticles in proximity to the surface. Conversely, as we distance ourselves from the surface, we observe an inverse trend, where the concentration rises with an increase in the Biot number.

Figure 6 depicts how the $\theta(\eta)$ and $\phi(\eta)$ profiles evolve as the Eckert number (Ec) increases. The observation shows that higher Eckert numbers lead to an increase in both the thickness of the fluid layer sticking to the surface and the temperature of the nanofluid. Consequently, this results in an improved TBL. Concerning the concentration of nanofluid, as the Eckert number rises, the layer of nanofluid adhering to the surface exhibits lower concentration. However, farther away from the sheet, the concentration behaves in the opposite manner.

Figure 7 underscores how the $\theta(\eta)$, and $\phi(\eta)$ fields are influenced by the thermophoresis parameter N_t when all other parameters are held constant. Both the temperature and the TBL of the nanofluid exhibit a mild increase in response to changes in the thermophoresis parameter, as observed. Higher values of the N_t result in an increased thermophoresis force. This force causes nanoparticles to diffuse in the surrounding fluid due to temperature gradients, leading to an elevated concentration of the nanofluid, particularly at a distance from the surface. However, a contrasting trend is observed near the surface. In a physical context, when the thermophoretic effect intensifies, it corresponds to a greater penetration of nanoparticles into the surrounding fluid. As a consequence, both the $\theta(\eta)$ and $\phi(\eta)$ of the nanofluid increase, leading to elevated levels of these properties.

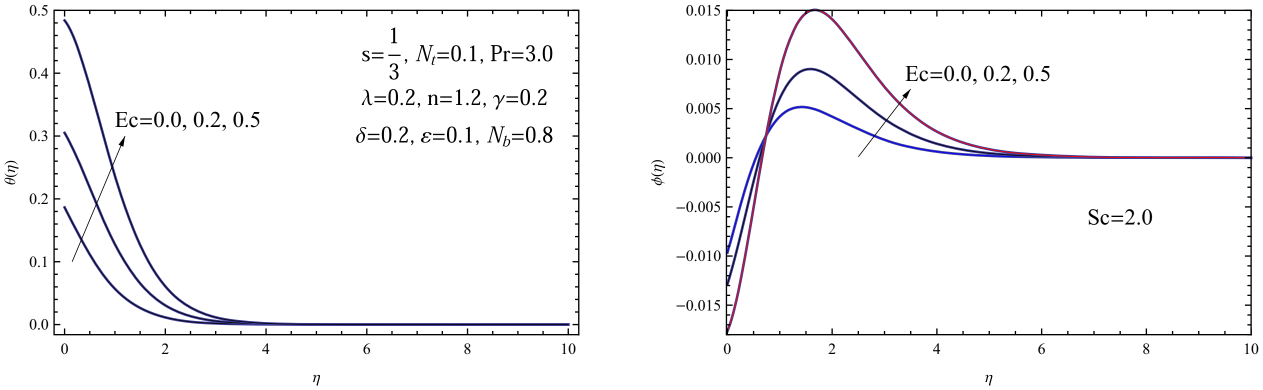

(a)

(b)

Figure 6: (a) $\theta(\eta)$ for various Ec and (b) $\phi(\eta)$ for various Ec.

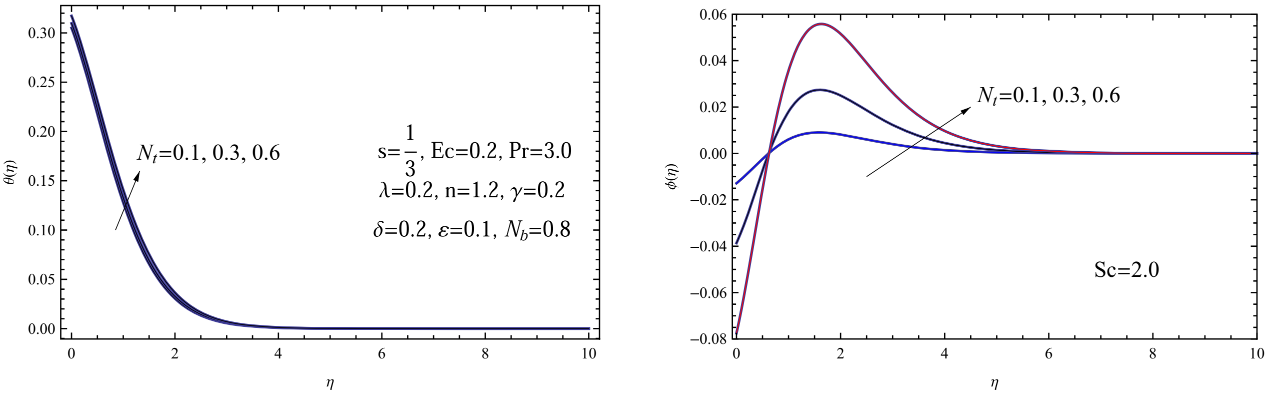

(a)

(b)

Figure 7: (a) $\theta(\eta)$ for various N_t and (b) $\phi(\eta)$ for various N_t.

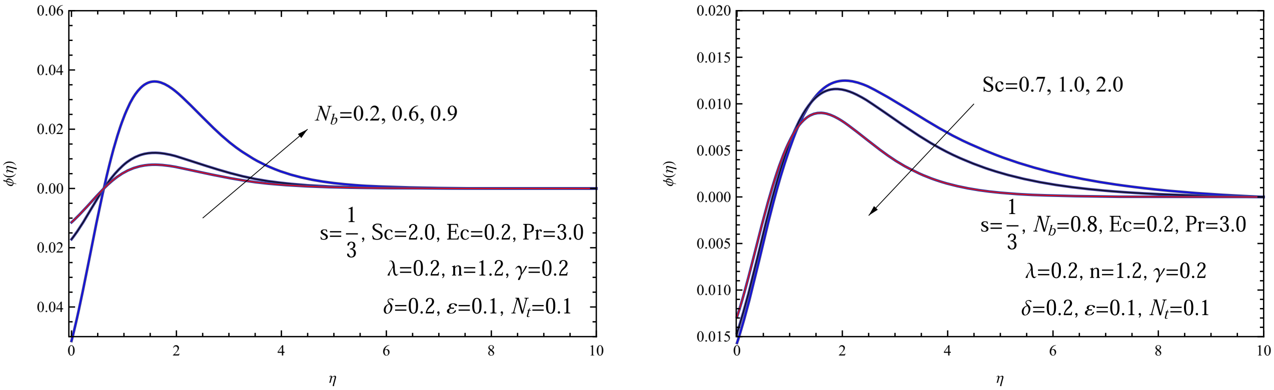

(a)

(b)

Figure 8: (a) $\phi(\eta)$ for various N_b and (b) $\phi(\eta)$ for various Sc.

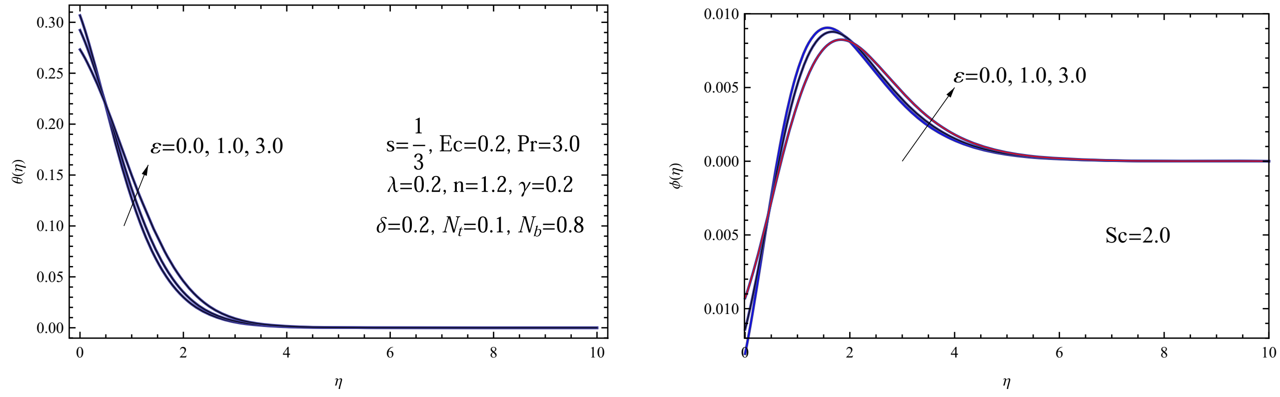

(a) (b)

Figure 9: (a) $\theta(\eta)$ for various ε and (b) $\phi(\eta)$ for various ε.

Table 3: Values of $\mathrm{Re}_x^{\frac{-1}{n+1}}\mathrm{Sh}_x$, $\mathrm{Re}_x^{\frac{-1}{n+1}}\mathrm{Nu}_x$, and $\frac{1}{2}\mathrm{Re}_x^{\frac{1}{n+1}}Cf_x$ for various values of $\delta, n, \lambda, \gamma$, Ec, N_t, N_b, and ε with Sc = 2.0, Pr = 3.0, and $s = \frac{1}{3}$

δ	n	λ	γ	Ec	N_t	N_b	ε	$\frac{1}{2}\mathrm{Re}_x^{\frac{1}{n+1}}Cf_x$	$\mathrm{Re}_x^{\frac{-1}{n+1}}\mathrm{Nu}_x$	$-\mathrm{Re}_x^{\frac{-1}{n+1}}\mathrm{Sh}_x$
0.0	1.2	0.2	0.2	0.2	0.1	0.8	0.1	0.529562	0.140718	0.0175897
0.2	1.2	0.2	0.2	0.2	0.1	0.8	0.1	0.628848	0.134881	0.0168601
0.5	1.2	0.2	0.2	0.2	0.1	0.8	0.1	0.751197	0.126876	0.0158596
0.2	0.6	0.2	0.2	0.2	0.1	0.8	0.1	0.786618	0.127690	0.0159612
0.2	0.9	0.2	0.2	0.2	0.1	0.8	0.1	0.691065	0.132701	0.0165876
0.2	1.2	0.2	0.2	0.2	0.1	0.8	0.1	0.628848	0.134881	0.0168601
0.2	1.2	0.0	0.2	0.2	0.1	0.8	0.1	0.766146	0.129807	0.0162258
0.2	1.2	0.2	0.2	0.2	0.1	0.8	0.1	0.628848	0.134881	0.0168601
0.2	1.2	0.4	0.2	0.2	0.1	0.8	0.1	0.537637	0.137577	0.0171971
0.2	1.2	0.2	0.1	0.2	0.1	0.8	0.1	0.628848	0.074908	0.0093635
0.2	1.2	0.2	0.2	0.2	0.1	0.8	0.1	0.628848	0.134881	0.0168601
0.2	1.2	0.2	0.4	0.2	0.1	0.8	0.1	0.628848	0.224913	0.0281141
0.2	1.2	0.2	0.2	0.0	0.1	0.8	0.1	0.628848	0.159732	0.0199665
0.2	1.2	0.2	0.2	0.2	0.1	0.8	0.1	0.628848	0.134881	0.0168601
0.2	1.2	0.2	0.2	0.5	0.1	0.8	0.1	0.628848	0.098448	0.0123060
0.2	1.2	0.2	0.2	0.2	0.1	0.8	0.1	0.628848	0.134881	0.0168601
0.2	1.2	0.2	0.2	0.2	0.3	0.8	0.1	0.628848	0.133913	0.0502174
0.2	1.2	0.2	0.2	0.2	0.6	0.8	0.1	0.628848	0.132347	0.0992606
0.2	1.2	0.2	0.2	0.2	0.1	0.2	0.1	0.628848	0.134881	0.0674405
0.2	1.2	0.2	0.2	0.2	0.1	0.6	0.1	0.628848	0.134881	0.0224802
0.2	1.2	0.2	0.2	0.2	0.1	0.9	0.1	0.628848	0.134881	0.0149868
0.2	1.2	0.2	0.2	0.2	0.1	0.8	0.0	0.628848	0.138658	0.0173323
0.2	1.2	0.2	0.2	0.2	0.1	0.8	1.0	0.628848	0.109531	0.0136914
0.2	1.2	0.2	0.2	0.2	0.1	0.8	3.0	0.628848	0.079891	0.0099864

Figure 8 illustrates the effect of the Schmidt (Sc) and Brownian motion N_b parameters on the nanoparticle concentration $\phi(\eta)$ profile. It is observed that, at a distance from the surface, increasing values of both the Sc, and N_b result in a decrease in nanoparticle concentration, leading to a reduction in the concentration BL. Conversely, near the surface, the opposite trend is noticed for both of these parameters.

Figure 9 presents $\theta(\eta)$ and $\phi(\eta)$ profiles for different values of the thermal conductivity parameter ε. This plot illustrates that at a distance from the stretching sheet, an increase in the values of the thermal conductivity parameter leads to an improvement in both the thermal and concentration fields of the nanofluid.

Table 3 displays numerical data for the skin friction coefficient $\frac{1}{2}\mathrm{Re}_x^{\frac{1}{n+1}}Cf_x$, local Sherwood number $\mathrm{Re}_x^{\frac{-1}{n+1}}\mathrm{Sh}_x$, and local Nusselt number $\mathrm{Re}_x^{\frac{-1}{n+1}}\mathrm{Nu}_x$ across various values of the governing parameters in the suggested model. It has been observed that the local Nusselt number exhibits a decreasing trend with respect to three factors: the n, λ, and the Biot number. Conversely, it shows an increasing trend with respect to three other factors: the δ, Ec, and N_t. In addition, it is noted that the skin friction coefficient rises as the δ increases, while it exhibits a decreasing trend with increasing values of both the n and λ. Moreover, the local Sherwood number experiences an increase as the n, λ, and Biot number rise, whereas the opposite trend is observed for the δ, Ec, and N_b.

7 Conclusion

Researchers are conducting a novel study, delving into the flow and heat transfer behaviors of a power-law nanofluid on a stretching sheet within a porous medium under convective heating. In addition, the study considered the effect of the slip velocity, and dissipative effects of viscosity. The analysis focuses on how changing thermal conductivity and nanoparticle control at the boundary influence the calculation. To obtain numerical solutions for the governing problem, we utilized a spectral collocation method that employs the sixth-order Chebyshev polynomials. We present visual representations illustrating how the pertinent parameters change concerning velocity, temperature, and nanoparticle concentrations. The key findings can be summarized as follows:

1) An increase in the n and λ led to a reduction in the thickness of the thermal and momentum BLs. Conversely, the concentration BL showed an opposite trend.
2) The presence of the porous parameter caused an increase in both temperature and nanoparticle concentration, while conversely, it led to a reduction in the velocity distribution.
3) An uptick in the Biot number and Eckert parameter led to higher nanofluid temperature, an increase in thermal thickness, and elevated sheet temperature.
4) Boosting thermophoretic forces resulted in a faster temperature rise across the TBL and led to an enhancement of nanoparticle concentration away from the sheet.
5) When the thermal conductivity parameter increased, the sheet's temperature decreased, but this trend reversed for the nanofluid as it moved away from the sheet.

Acknowledgments: The authors extend their appreciation to the Deputyship for Research & Innovation, Ministry of Education in Saudi Arabia for funding this research through the project number IFP-IMSIU-2023055. The authors also appreciate the Deanship of Scientific Research at Imam Mohammad Ibn Saud Islamic University (IMSIU) for supporting and supervising this project.

Funding information: This research was funded by the Deputyship for Research & Innovation, Ministry of Education in Saudi Arabia through the project number IFP-IMSIU-2023055. The authors also appreciate the Deanship of Scientific Research at Imam Mohammad Ibn Saud Islamic University (IMSIU) for supporting and supervising this project.

Author contributions: All authors have accepted responsibility for the entire content of this manuscript and approved its submission.

Conflict of interest: The authors state no conflict of interest.

References

[1] Lakshmisha KN, Venkateswaran S, Nath G. Three-dimensional unsteady flow with heat and mass transfer over acontinuous stretching surface. ASME J Heat Transfer. 1988;110:590–5.
[2] Krishna MV, Ahammad NA, Chamkha AJ. Radiative MHD flow of Casson hybrid nanofluid over aninfinite exponentially accelerated vertical porous surface. Case Studies Thermal Eng. 2021;27:1–15.
[3] Madhua M, Kishana N, Chamkha AJ. Unsteady flow of a Maxwell nanofluid over a stretching surface in thepresence of magnetohydrodynamic and thermal radiation effects. Propulsion Power Res. 2017;6(1):31–40.
[4] Magyari E, Chamkha AJ. Combined effect of heat generation or absorption and first-order chemical reactionon micropolar fluid flows over a uniformly stretched permeable surface: The full analytical solution. Int J Thermal Sci. 2010;49(9):1821–8.
[5] Shafiq A, Sindhu TN. Statistical study of hydromagnetic boundary layer flow of Williamson fluid regarding a radiative surface. Results Phys. 2017;7:3059–67.
[6] Shafiq A, Oudina FM, Sindhu TN, Abidi A. A study of dual stratification on stagnation point WalterasB nanofluid flow via radiative Riga plate: a statistical approach. Europ Phys J Plus. 2021;136(407):1–24.
[7] Shafiq A, Sindhu TN, Khalique CM. Numerical investigation and sensitivity analysis on bioconvectivetangent hyperbolic nanofluid flow towards stretching surface by response surface methodology. Alexandr Eng J. 2020;59(6):4533–48.
[8] Shafq A, Lone SA, Sindhu TN, Al-Mdallal QM, Rasool G. Statistical modeling for bioconvectivetangent hyperbolic nanofuid towards stretching surface with zero mass flux condition. Scientific Reports 2021;11(13869):1–11.
[9] Schowalter WR. The application of boundary layer theory to power-law pseudoplastic fluids: similar solution. AIChE J 1960;6:24–8.

[10] Ariel PD. On the flow of power law fluid over a stretching sheet-techniques and solutions. Acta Mechanica 2002;156:13–27.

[11] Mahmoud MAA, Megahed AM. Effects of viscous dissipation and heat generation (absorption) in a thermal boundary layer of a non-Newtonian fluid over a continuously moving permeable flat plate. J Appl Mechanics Technical Phys. 2009;156:819–25.

[12] Sui JZ, Zheng LC, Zhang XX, Chen G. Mixed convection heat transfer in power-law fluids over a movingconveyor along an inclined plate. Int J Heat Mass Transfer. 2015;85:1023–33.

[13] Megahed AM. Flow and heat transfer of a non-Newtonian power-law fluid over a non-linearly stretching vertical surface with heat flux and thermal radiation. Meccanica. 2015;50:1693–700.

[14] Choi S. Enhancing thermal conductivity of fluid with nanoparticles, developments and applications of non-Newtonianflow. ASME FED 1995;231:99–105.

[15] Masuda H, Ebata A, Teramae K, Hishinuma N. Alteration of thermal conductivity and viscosity of liquid bydispersing ultra-fine particles. Netsu Bussei. 1993;7:227–33.

[16] Aziz A, Khan WA. Natural convective boundary layer flow of a nanofluid past a convectively heated vertical plate. Int J Therm Sci. 2012;52:83–90.

[17] Alali E, Megahed MA. MHD dissipative Casson nanofluid liquid film flow due to an unsteady stretching sheet with radiation influence and slip velocity phenomenon. Nanotechnol Rev. 2022;11:463–72.

[18] Saad KM, Khader MM, Gomez-Aguilar JF, Dumitru B. Numerical solutions of the fractional Fisheras typeequations with Atangana-Baleanu fractional derivative by using spectral collocation methods. Chaos. 2019;29:1–5.

[19] Khader MM, Saad KM. A numerical approach for solving the problem of biological invasion (fractional Fisher equation)using Chebyshev spectral collocation method. Chaos Solitons Fractals. 2018;110:169–77.

[20] Atta AG, Moatimid GM, Youssri YH. Generalized Fibonacci operational collocation approach for fractional initial value problems. Int J Appl Comput Math. 2019;5:1–9.

[21] Atta AG, Abd-Elhameed WM, Moatimid GM, Youssri YH. Advanced shifted sixth-kind Chebyshev tau approach forsolving linear one-dimensional hyperbolic telegraph type problems. Math Sci. 2022;6:1–15.

[22] Megahed AM. Variable viscosity and slip velocity effects on the flow and heat transfer of a power-law fluidover a non-linearly stretching surface with heat flux and thermal radiation. Rheologica Acta. 2012;51:841–74.

[23] Megahed AM. Improvement of heat transfer mechanism through a Maxwell fluid flow over a stretching sheet embedded in a porous medium and convectively heated. Math Comput Simulat. 2021;187:97–109.

[24] Mahmoud MAA, Megahed AM. Non-uniform heat generation effects on heat transfer of a non-Newtonian fluid over a non-linearly stretching sheet. Meccanica. 2012;47:1131–9.

[25] Khan M, Khan WA. MHD boundary layer flow of a power-law nanofluid with new mass flux condition. AIP Adv. 2016;6:025211.

[26] Boyd JP. Chebyshev and Fourier spectral methods, 2nd ed. New York, USA: Dover; 2000.

[27] Snyder MA. Chebyshev methods in numerical approximation, Prentice-Hall, Inc Englewood Cliffs: NJ; 1966.

[28] Khader MM, Saad KM. On the numerical evaluation for studying the fractional KdV, KdV-Burgeras, and Burgeras equations. Europ Phys J Plus. 2018;133:1–13.

[29] Mason JC, Handscomb DC. Chebyshev polynomials. New York, NY, Boca Raton: Chapman and Hall, CRC; 2003.

[30] Abd-Elhameed WM, Youssri YH. Sixth-kind Chebyshev spectral approach for solving fractional differential equations. Int J Nonlinear Sci Numer Simul. 2019;20:191–203.

[31] Atta A, Abd-Elhameed WM, Moatimid G, Youssri YH. A fast Galerkin approach for solving the fractionalRayleigh-Stokes problem via sixth-kind Chebyshev polynomials. Mathematics. 2022;10:1843.

[32] El-Hawary HM, Salim MS, Hussien HS. Ultraspherical integral method for optimal control problems governed by ordinary differential equations. J Glob Optim. 2003;25:283–303.

[33] Hassanien IA, Abdullah AA, Gorla RSR. Flow and heat transfer in a power-law fluid over a nonisothermal stretching sheet. Math Comput Modell. 1998;28:105–16.

[34] Khan WA, Gorla RSR. Heat and mass transfer in power-law nanofluids over a nonisothermal stretching wall with convective boundary condition. J Heat Transfer. 2012;134:112001.

[35] Gorla RSR, Chamkha AJ. Natural convective boundary layer flow over a nonisothermal vertical plate embedded in a porous medium saturated with a nanofluid. Nanoscale Microscale Thermophys Eng. 2011;15(2):81–94.